The Cryosphere Discuss., https://doi.org/10.5194/tc-2018-248
Manuscript under review for journal The Cryosphere
Discussion started: 13 December 2018
© Author(s) 2018. CC BY 4.0 License.

The Cryosphere Discussions
Open Access
EGU

Identification of blowing snow particles in images from a multi-angle snowflake camera

Mathieu Schaer[1], Christophe Praz[1], and Alexis Berne[1]

[1] Environmental Remote Sensing Laboratory, École Polytechnique Fé dérale de Lausanne, Switzerland

Correspondence: Alexis Berne (alexis.berne@epfl.ch)

Abstract. A new method to automatically discriminate between hydrometeors and blowing snow particles on Multi-Angle Snowflake Camera (MASC) images is introduced. The method uses four selected descriptors related to the image frequency, the number of particles detected per image as well as their size and geometry to classify each individual image. The classification task is achieved with a two components Gaussian Mixture Model fitted on a subset of representative images of each class from field campaigns in Antarctica and Davos, Switzerland. The performance is evaluated by labelling the subset of images on which the model was fitted. An overall accuracy and Cohen's Kappa score of 99.4 and 98.8%, respectively, is achieved. In a second step, the probabilistic information is used to flag images composed of a mix of blowing snow particles and hydrometeors, which turns out to occur frequently. The percentage of images belonging to each class from an entire austral summer in Antartica and during a winter in Davos, respectively, are presented. The capability to distinguish precipitation, blowing snow and a mix of those in MASC images is highly relevant to disentangle the complex interactions between wind, snowflakes and snowpack close to the surface.

Copyright statement. TEXT

1 Introduction

Over snow covered regions, ice particles can be lifted from the surface by the wind and suspended in the atmosphere. Wind-driven snow transport is ubiquitous in the cryosphere: over complex terrain (e.g. Winstral et al., 2002; Mott and Lehning, 2010), over toundra/prairies (e.g. Pomeroy and Li, 2000) and over polar ice sheets (e.g. Bintanja, 2001; Déry and Yau, 2002; Palm et al., 2011). Wind-driven snow transport must be taken into account to obtain accurate estimates of the mass balance and radiative forcings at the surface (e.g. Gallée et al., 2001; Lesins et al., 2009; Scarchilli et al., 2010; Yang et al., 2014). In mountainous regions, wind-transported snow also creates local accumulations and irregular deposits, being a critical factor influencing avalanche formation (e.g. Schweizer et al., 2003). Quantifying snow transport during snowfall events and subsequent periods of strong winds is essential for local avalanche prediction (e.g. Lehning and Fierz, 2008). In the context of climate change, the mass balance of the Antarctic ice sheet is of increasing relevance due to its impact on sea level rise (Shepherd et al., 2012). The sustained katabatic winds in Antarctica generate frequent blowing snow events, that remove a significant amount

© Author(s) 2018. CC BY 4.0 License.

of new snow through transport and sublimation. Wind-transported snow is hence an important factor to take into account when considering Antarctic mass balance (e.g. Déry and Yau, 2002; Scarchilli et al., 2010; Lenaerts and van den Broeke, 2012; Das et al., 2013). Blowing snow is also an important process for the mass balance of the Greenland ice sheet (e.g. Box et al., 2006).

The layers formed by wind-suspended ice particles are commonly separated in two classes: drifting snow when the top of this layer is less than 2 m above ground, blowing snow above (see http://glossary.ametsoc.org for instance). The present study focuses on blowing snow because the observations used for detection were collected more than 2 m above ground (but the proposed approach could easily be extended to drifting snow if relevant data are collected/available).

Blowing snow is challenging to measure and characterize. Various approaches have been proposed to monitor blowing snow at ground level: mechanical traps, nets, photoelectric or acoustic sensors, photographic systems (see Leonard et al., 2012, for a more detailed review). Remote sensing, and lidar systems in particular, have recently been used to characterize the occurrence and depth of blowing snow layers, either from space Palm et al. (2011) or near ground-level Gossart et al. (2017). Suspended ice particles are under the influence of the gravitational force, proportional to the size cubed while the drag force is proportional to the area (size squared). With a greater area to mass ratio, smaller particles are thus more likely to be lifted in the suspension layer. A comparison of ten different studies of measured and simulated particle size distributions of blowing snow, reveals mean diameters at heights above $0.2\,\mathrm{m}$ ranging from 50 to $160\,\mu\mathrm{m}$ (Gordon and Taylor, 2009).

Blowing snow may also contaminate precipitation observations collected by ground-based sensors, obviously in Antarctica (e.g. Gossart et al., 2017) where winds are strong and frequent, but also in snowy regions in general (Rasmussen et al., 2012; Scaff et al., 2015). The issue of snowfall measurement is complex and WMO promoted intercomparison projects to evaluate various sensors and define standards set-ups and protocols over the last two decades, as illustrated in (Goodison et al., 1998) and the recent SPICE project (http://www.wmo.int/pages/prog/www/IMOP/intercomparisons/SPICE/SPICE.html).

The Multi-Angle Snowflake Camera (MASC) is a ground-based instrument designed to automatically captures high resolution ($\sim 33.5\,\mu\mathrm{m}$) photographs of falling hydrometeors from three different angles (Garrett et al., 2012). The MASC has been used in prevuous studies to investigate snowflake properties (Garrett et al., 2015; Grazioli et al., 2017) and to help interpret weather radar measurements (Kennedy et al., 2018). Interestingly, blowing snow particles also trigger the motion detector system, producing many images in windy environments. Combined with the hydrometeor classification techniques based on MASC images (e.g. Praz et al., 2017), the ability to discriminate between images composed of blowing snow and precipitation particles is therefore relevant to characterize blowing snow, to provide reference observations to improve its remote sensing, as well as to obtain more accurate snowfall estimates from ground-based sensors. More generally, detailed information about the type of particles pictured by a MASC will enable us to further investigate the complex interactions between wind, snowflakes and snowpack close to the surface in cold and windy regions.

This article presents a new method to automatically determine if an image from the MASC (and potentially other imaging instruments) is composed of blowing snow particles, precipitating hydrometeors (snowflakes and ice crystals) or a mix of both. The classification is accomplished by means of a Gaussian mixture model (GMM) with two components, fitted on a set of representative MASC images and evaluated on a manually-built validation set. The paper is organized as follows: Section 2 introduces the data sets used to develop the method and fit the GMM. Section 3 illustrates the different steps to isolate the

The Cryosphere Discuss., https://doi.org/10.5194/tc-2018-248
Manuscript under review for journal The Cryosphere
Discussion started: 13 December 2018
© Author(s) 2018. CC BY 4.0 License.

Figure 1. Experimental set-up conditions of the MASC in a DFIR near Davos (left) and on top of a container at DDU (right).

particles and extract related features for the clustering task. Section 4 explains the selection of the most relevant features, the fitting of the GMM as well as the attribution of a flag for mixed images. The main results are shown in Section 5. At last, limitations and further improvements are discussed in Section 6.

2 Data sets

The MASC data used to implement and validate the present algorithm were collected during three field campaigns. The first one took place in Davos, Switzerland during the winter 2015-2016. The MASC was placed at 2540 m a.s.l in a Double Fence Intercomparison Reference (DFIR, see Fig. 1, left), designed to limit the adverse effect of wind on the measuring instruments in its center (Goodison et al., 1998). The two other campaigns took place at the French Antarctic Dumont d'Urville station, on the coast of Adelie Land, during the austral summer 2015-2016 and from January to July 2017 in the framework of the Antarctic Precipitation, Remote Sensing from Surface and Space project[1] (Grazioli et al., 2017; Genthon et al., 2018). The instrument was deployed on a rooftop at about 3 m above ground (see Fig. 1, right). A collocated weather station and a micro rain radar (MRR) were also installed. Nearly three millions images were collected during these measurement campaigns all together.

From this great amount of data, subsets of pure precipitation and pure blowing snow images were manually selected and further analyzed to chose relevant descriptors and fit a two components GMM. The task of selecting enough representative images from both class appeared less trivial than expected, especially for Antarctica, as mixed images are especially common. Gossart et al. (2017) used ceilometer data collected at the Neumayer and Princess Elizabeth stations in East Antarctica to investigate blowing snow, and they suggests that more than 90% of blowing snow occurs during synoptic events, usually combined with precipitation. For the sake of generalization, as many representative events as possible were selected across the three campaigns. The goal was to cover a wide range of hydrometeors types as well as snowfall rate for the precipitation

[1] http://apres3.osug.fr

© Author(s) 2018. CC BY 4.0 License.

Table 1. Campaigns and dates of selected events for the Blowing snow (BS) and Precipitation (P) subsets.

Antarctica 15-16	Antarctica 17	Davos 15-16
11 Nov BS	08 Feb BS	23 Feb P
22 Nov P	09 Feb BS	25 Feb P
15 Dec P	18 Feb BS	04 Mar P
16 Dec P	19 Feb BS	05 Mar P
30 Dec P		16 Mar P
02 Jan P		25 Mar P
11 Jan P		
28 Jan BS		

subset. Similarly, varying wind speeds and concentration densities were considered to build the blowing snow subset. From the campaigns in Antarctica, pure blowing snow and hydrometeors events were highlighted by comparing time series of MASC image frequency, wind speed and MRR derived rain rate, as illustrated in Figure 2. It was noticed that during strong blowing snow events, the number of images captured by the MASC was exceptionally important. Potential pure blowing snow events were selected when the MASC image frequency and wind speed were higher than their respective median observed over the whole campaign and no precipitation was detected during the preceding hour. Only events for which these criteria applied for over an hour consecutively were kept. To highlight pure precipitation, the principle was the same but the criteria were an image frequency and a wind speed lower than the median and a MRR precipitation rate greater than zero. The MRR has a certain detection limit, so it was noticed that events selected as blowing snow could also occur during undetected light precipitation. As a result, images from all events were rapidly checked vizually and the campaign logbook consulted to ensure that the selection was consistent and coherent. In both cases, some events had to be removed because of obvious mixing of blowing snow and hydrometeors.

As the MASC was deployed inside a DFIR in Davos, no blowing snow events were selected from this campaign. Although the DFIR is supposed to shelter the inner instruments from wind disturbances, we noticed that many images do not solely contain pure hydrometeors. From a webcam monitoring the instrumental set up, one could notice that the fresh snow accumulated on the edges and borders of the wooden structure of the DFIR was frequently blown away towards the sensor. To augment the precipitation subset, events with high snowfall rate but not affected by outliers of fresh wind-blown snow were added. Finally, some sparse images of obvious pure hydrometeor in the middle of mixed events were also included in the training set. In total, each subset contained 4263 images and is assumed to be accurate and reliable enough to serve as reference for the evaluation of the proposed technique (see Fig. 7 and Section 4.2).

The Cryosphere Discuss., https://doi.org/10.5194/tc-2018-248
Manuscript under review for journal The Cryosphere
Discussion started: 13 December 2018
© Author(s) 2018. CC BY 4.0 License.

The Cryosphere
Discussions
Open Access

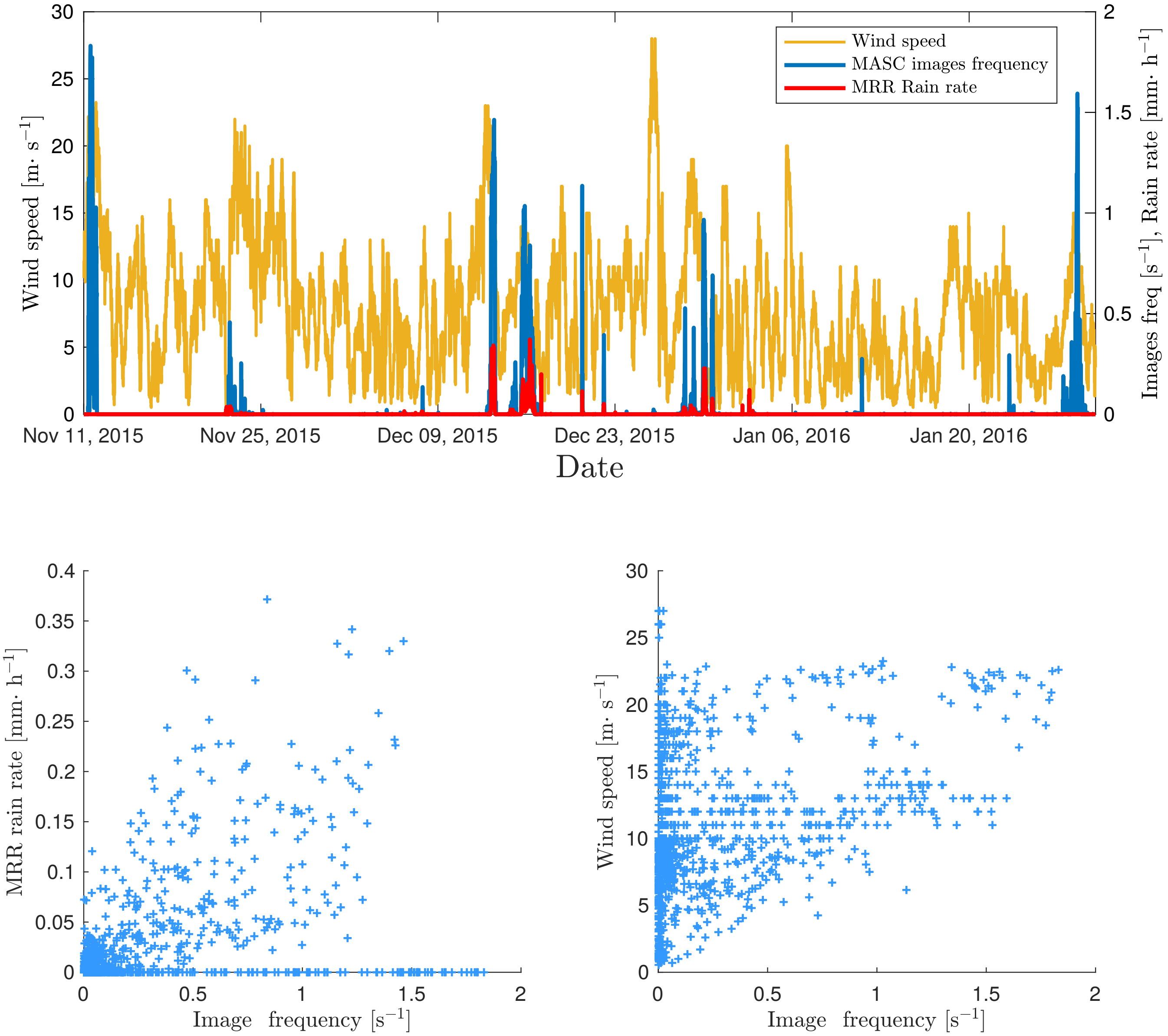

Figure 2. Time series and scatter plots of MASC image frequency, wind speed and MRR derived rain rate for the Antarctica 2015-2016 campaign. Points on the x-axis in the left scatter plot are potential candidates for pure blowing snow.

The Cryosphere Discuss., https://doi.org/10.5194/tc-2018-248
Manuscript under review for journal The Cryosphere
Discussion started: 13 December 2018
© Author(s) 2018. CC BY 4.0 License.

3 Image Processing

3.1 Particles detection

The MASC consists of three cameras mounted on a ring structure with an angle of 36° between them and sharing the same focal point in the middle of the ring. The motion detector system is composed of two horizontally aligned near-infrared emitter-receiver arrays, which delimit a $8.3\,\mathrm{cm}^2$ detection surface in the center of the structure, where the two beams overlap (see Garrett et al., 2012, for more details). A particle passing through this area triggers the cameras together with three spotlights that illuminate the target. In the present study, all images have a size of 2448×2048 pixels.

Although a single particle activates the cameras, many MASC pictures contain multiple particles distributed over the entire image, especially when blowing snow occurs. In fact, the number of particles appearing on a single image is a key characteristic to distinguish between precipitation and blowing snow. As a result, it was deemed essential to detect all particles in each image rather than the triggering one only (which is sometimes unidentifiable). A key challenge of this approach was to get rid of the noisy background. For this purpose, a median filter was used. The brightness of the background strongly depends on the luminosity at the instant of the picture, which varies according to the time of day and can change abruptly in partly cloudy conditions when the sun suddenly appears from behind a cloud. As a result, the median filter shows better performance to remove the background when systematically re-computed over a small number of consecutive images. Assuming that snow particles hardly appear at the exact same position on few consecutive images, the median filter was chosen to be computed over blocks of 5 images per camera angle. To ensure complete removal of the background when its brightness is greater that the corresponding median, a factor of 1.1 was applied to the filter. Finally, as some limited residual noise can still remain in the filtered image, a small detection threshold of 0.02 grayscale intensity was applied to isolate the snow particles. Masks of the sky and reflecting parts of the background (i.e. metallic plates etc) were created for each camera. The multiplication factor and detection threshold are increased in the regions delineated by the masks if the normal filtering leads locally to more pixels detected that one can expect from real particles. These steps are illustrated in Figures 3 and 4. Issues in the filtering may occur if consecutive images are separated by a too long period of time, during which the ambient luminosity has changed significantly (e.g. before/after the sunrise or sunset). An example is shown in Figure B1 in Appendix B.

3.2 Feature extraction

Machine learning algorithms require a set of variables, commonly called features or descriptors, upon which the classification is performed. In this study, various quantitative descriptors were calculated according to four different categories: the number of particles and their spread across the image, the size of the particles, the geometry of the particles and the frequency at which the images are taken. Since it is difficult to exactly guess which descriptors are the most adequate to differentiate between blowing snow and precipitation images, an extensive collection of features was extracted from the blowing snow and precipitation subsets and compared. The selection of the most relevant ones is explained in the next section. As the classification is performed at the image level, the information on the geometry and size of each detected particle in the image was transformed into a single descriptor. Consequently, quantiles ranging from 0 to 1 and moments from 1 to 10 were computed out of the distribution of

© Author(s) 2018. CC BY 4.0 License.

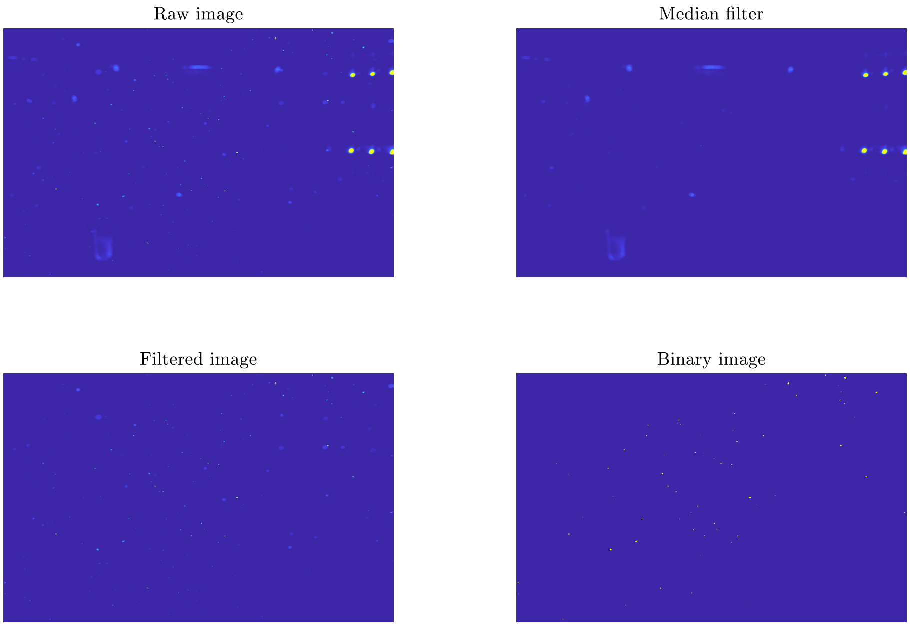

Figure 3. Raw image, median filter, filtered image and final binary image for an example of blowing snow particles. The color scheme is used to enhance details for visual purposes.

the considered feature within the image. The image frequency is a descriptor independent from the content of the image and thus from the detection of particles. It is therefore not affected by potential image processing issues. As each image comes with its attributed timestamp, the average number of images per minute was calculated with a moving window. The full list of all computed descriptors is displayed in Appendix A. The extraction of features was conducted with the `MATLAB` Image Processing Toolbox, in particular the function `regionprops`[2].

4 Classification

4.1 Feature selection and transformation

Selecting a pertinent set of features and avoiding redundancy is essential for accurate classification, regardless of the classification algorithm. For each of the four categories of descriptors previously mentioned, the most relevant one was kept. The descriptor maximizing the “inter-clusters over intra-clusters" distance described in Eq. 1 was selected. This quantity represents the distance between the mean of the blowing snow and precipitation distributions (μ_{BS} and μ_P respectively), normalized by the sum of their respective standard deviations (σ_{BS} and σ_P respectively).

$$S = \frac{|\mu_{BS} - \mu_P|}{\frac{1}{2}(\sigma_{BS} + \sigma_P)}. \tag{1}$$

[2] https://ch.mathworks.com/help/images/ref/regionprops.html

The Cryosphere Discuss., https://doi.org/10.5194/tc-2018-248
Manuscript under review for journal The Cryosphere
Discussion started: 13 December 2018
© Author(s) 2018. CC BY 4.0 License.

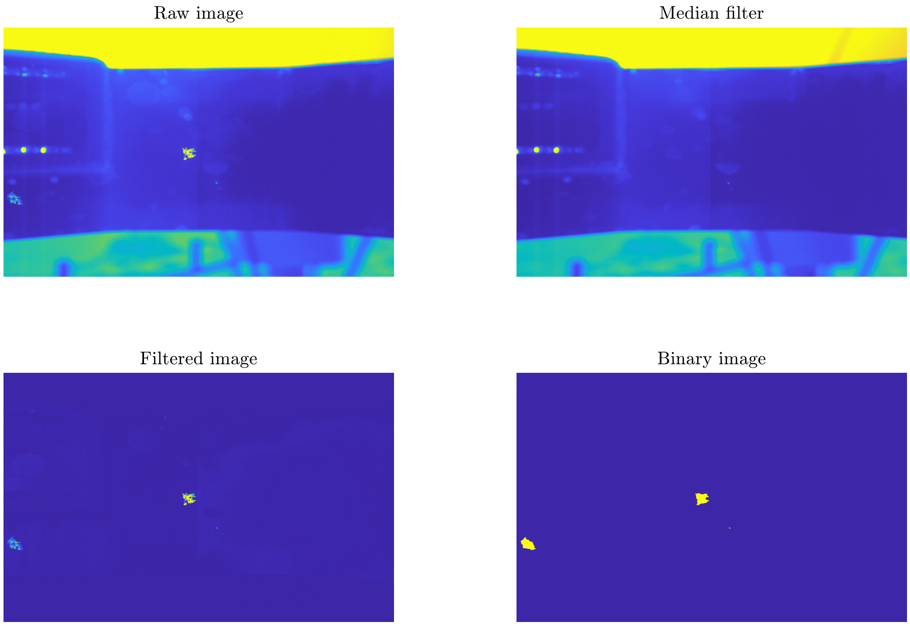

Figure 4. Raw image, median filter, filtered image and final binary image for an example of hydrometeor. The color scheme is used to enhance details for visual purposes.

For the features describing the number of detected particles and their spread across the image, the *cumulative distance transform* was kept. It represents the sum over each entry of the distance transform matrix[3]of the binary image. The distance transform matrix has the same dimensions as the binary image and computes, for each pixel, the Euclidean distance to the nearest 1 element (i.e. the nearest particle). As a result, an image with many particles well distributed over its entire surface will have a low *cumulative distance transform*, while a single particle, even particularly large, will have a high value. This descriptor is more robust to image processing issues than the raw number of particles, as illustrated in Figure B2 in Appendix B.

Concerning the size distribution of the particles detected in an image, the quantile 0.7 of the maximum diameter was selected. The maximum diameter (*Dmax*) represents the longest segment between two edges of a particle (see Praz et al., 2017, for more details). A logarithmic transformation of this feature was performed to make the distributions of the two classes more Gaussian. The minimum (i.e. quantile 0) squared fractal index showed the greatest S value (hence discrimination potential) among the features related to the particle geometry indices. The fractal index (FRAC) is defined according to the formula proposed by McGarigal and Marks (1995) in the context of landscape pattern analysis. It was also more recently used to quantify stand structural complexity from terrestrial laser scans of forests (Ehbrecht et al., 2017).

Due to its different nature, the image frequency descriptor was selected by default, but it is worth noting that it has the highest S value (Eq. 1) among all descriptors (Table 2).

[3]https://ch.mathworks.com/help/images/ref/bwdist.html

The Cryosphere Discuss., https://doi.org/10.5194/tc-2018-248
Manuscript under review for journal The Cryosphere
Discussion started: 13 December 2018
© Author(s) 2018. CC BY 4.0 License.

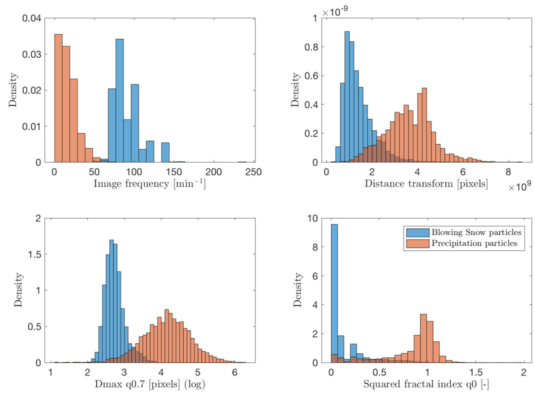

Figure 5. Histograms of selected descriptors for the blowing snow and precipitation subsets.

Table 2. Selected features and corresponding S values

Feature name	S
Image frequency	4.43
Cumulative distance transform	2.89
Maximum diameter quantile 0.7	1.71
Squared fractal index quantile 0	3.81

4.2 Model fitting

The choice for the binary classification task was made on a Gaussian mixture model, an unsupervised learning technique that fits a mixture of multivariate Gaussian distributions to the data (see Murphy, 2012; McLachlan and Basford, 1988; Moerland, 2000, for more details). The mathematical description of a multivariate normal distribution is provided in Eq. 2. The justification for the unsupervised approach is manifold. First, unsupervised methods do not depend upon labels. Hence, it is not required to ensure correct labelling of each image in the training set. As mentioned earlier, many images are composed of mix of blowing snow and precipitation and it is thus difficult to guarantee the objectivity of all given labels. Second, a clear separation observed between the two subsets would be statistically highly significant as no prior information is provided to the learning algorithm about the classes. Third, for low dimensional problems, unsupervised methods are sometimes less prone to over-fitting and have a better potential of generalization. A main advantage of the GMM compared to other unsupervised methods is to provide posterior probabilities on the cluster assignments and thus allow for soft clustering. In the context of the present study, this is absolutely relevant as there exists a whole continuum of in-between cases of mixed images. It should be noted that the

The Cryosphere Discuss., https://doi.org/10.5194/tc-2018-248
Manuscript under review for journal The Cryosphere
Discussion started: 13 December 2018
© Author(s) 2018. CC BY 4.0 License.

descriptors were selected using a reference set (see previous section), but the clustering conducted by means of the GMM is itself unsupervised.

$$\mathcal{N}(x|\mu,\Sigma) = \frac{1}{(2\pi)^{D/2}|\Sigma|^{1/2}}\exp\{-\frac{1}{2}(x-\mu)^T\Sigma^{-1}(x-\mu)\}. \quad (2)$$

A two components GMM with unshared full covariance matrices was thus fitted to the four dimensional data composed of the blowing snow and precipitation subsets. The MATLAB Statistics and Machine Learning Toolbox was used to this purpose and the model parameters were estimated by maximum likelihood via the Expectation-Maximization (EM) algorithm[4]. The features were standardized before fitting the model. The mixing weights (or component proportions) were artificially set to 0.5 by randomly removing 80 data points from the training set and fitting again the GMM to have perfectly balanced classes. This step is essential as the model will then be used to classify new images (possibly from other campaigns). There are no reasons to give more weight to one component, as the relative proportion of blowing snow and precipitation images strongly depends on the campaign location. The posterior probabilities are computed using Bayes rule (Murphy, 2012):

$$P(z_i = k|\boldsymbol{x}_i,\boldsymbol{\theta}) = \frac{P(\boldsymbol{x}_i|z_i = k,\boldsymbol{\theta})P(z_i = k|\boldsymbol{\theta})}{P(\boldsymbol{x}_i|\boldsymbol{\theta})}, \quad (3)$$

where z_i is a discrete latent variable taking the values $1,...,K$ and labelling the K Gaussian components. $P(z_i = k|\boldsymbol{x}_i,\boldsymbol{\theta})$ is the posterior probability that point i belongs to cluster k (also known as the "responsibility" of cluster k for point i). $P(\boldsymbol{x}_i|z_i = k,\boldsymbol{\theta})$ corresponds to the density of component k at point i (i.e. $\mathcal{N}(\boldsymbol{x}_i|\boldsymbol{\mu}_k,\boldsymbol{\Sigma}_k)$) and $P(z_i = k|\boldsymbol{\theta})$ represents the mixing weight (also denoted π_k). Note that the π_k are positive and sum to 1. $\boldsymbol{\theta}$ refers to the fitted parameters of the mixture model $\{\boldsymbol{\mu}_1,...,\boldsymbol{\mu}_k,\boldsymbol{\Sigma}_1,...,\boldsymbol{\Sigma}_K,\pi_1,...,\pi_K\}$. $P(\boldsymbol{x}_i|\boldsymbol{\theta})$ is the marginal probability at point i, which is simply the weighted sum of all component densities:

$$P(\boldsymbol{x}_i|\boldsymbol{\theta}) = \sum_{k=1}^{K}\pi_k\mathcal{N}(\boldsymbol{x}_i|\boldsymbol{\mu}_k,\boldsymbol{\Sigma}_k). \quad (4)$$

As the concern of this study is on two components only, a more compact notation will be used for the rest of the article. The latent variable z will be replaced by k_P and k_{BS} to refer to the precipitation and blowing snow clusters, respectively. The term $\boldsymbol{\theta}$, that denotes the model parameters, will be left implicit. Assuming we are at first interested by performing some hard clustering, an image will be classified as blowing snow if $P(k_{BS}|\boldsymbol{x}_i) > P(k_P|\boldsymbol{x}_i)$. In words, if the posterior probability to belong to the blowing snow cluster is greater than 0.5, an image will be classified as such (because the posterior probabilities sum to 1). The model performance was assessed by simply labelling the data points according to its initial subset. An overall accuracy of 99.4% and a Cohen's Kappa score of 98.8% were achieved. The Cohen's Kappa statistic adjusts the accuracy by accounting for correct predictions occurring by chance (Byrt et al., 1993). To investigate the stability of the Gaussian components, the precipitation and blowing snow subsets were both randomly permuted and divided in ten equal parts. Ten new

[4]https://ch.mathworks.com/help/stats/gaussian-mixture-models-2.html

The Cryosphere Discuss., https://doi.org/10.5194/tc-2018-248
Manuscript under review for journal The Cryosphere
Discussion started: 13 December 2018
© Author(s) 2018. CC BY 4.0 License.

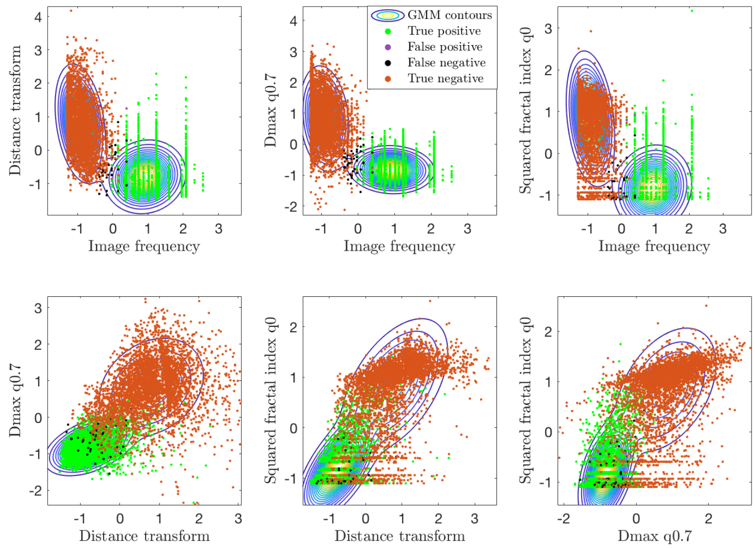

Figure 6. GMM contours and data points projected on the 2D planes. The colors correspond to the four entries of the confusion matrix. The predictions result from the clustering and the ground truth is the given labels.

training sets of balanced amount of each subset were created and new GMM fitted. Figure 7 shows on the top line the boxplots of the Gaussian components parameters $\boldsymbol{\mu}_d$ and $\boldsymbol{\sigma}_d$ (i.e. diagonal entries of $\boldsymbol{\Sigma}$) for each of the four dimensions. The boxplots show a limited variability for each feature (below 10%), indicating a reasonable stability of the fitted parameters. In addition, the bottom line of Figure 7 presents the learning curves, and their fast convergence to the same horizontal line when more than 30% of the training set is used, indicates a training set large enough for a reliable fitting of the GMM, without overfitting.

4.3 Flag for mixed images

As mentioned earlier, an asset of using a GMM model is the posterior probabilistic information that could help estimate the degree of mixing of an image. Data points located close to the decision boundary in the multidimensional space are likely to be composed of a mix of blowing snow particles and hydrometeors. However, distributions of posterior probabilities computed over thousands of new images from entire campaigns, showed that they were stretched out on both end of the domain (i.e. close to 0 or 1) and not many images were present in between. This is probably due to the nature of the descriptors and the resulting shapes and relative positions of the Gaussian distributions. Nevertheless, a subset of mixed images, specially created for this purpose, highlighted clear discrepancies on the posterior probabilities with the pure blowing snow and precipitation subsets. However, this differentiation was around 10^{-6} (or $1-10^{-6}$), which is not so informative as such. Consequently, it was decided to define a new index, similar to the posterior probability to belong to the blowing snow component, but more evenly distributed across the range $]0,1[$. The new index uses the negative logarithm of the posterior probabilities multiplied by the

The Cryosphere Discuss., https://doi.org/10.5194/tc-2018-248
Manuscript under review for journal The Cryosphere
Discussion started: 13 December 2018
© Author(s) 2018. CC BY 4.0 License.

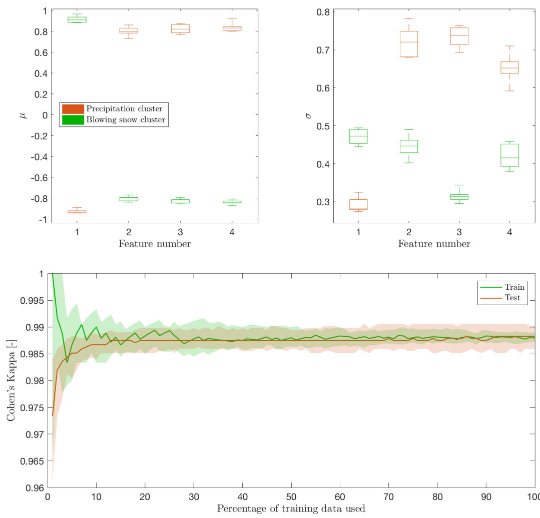

Figure 7. Top: stability of the parameters μ and σ (diagonal entries of $\mathbf{\Sigma}$) for the two Gaussian components. The boxplots show the distributions of these parameters for each dimension, after fitting the GMM on a 10-fold random split of the training set. The feature number follows the order given in Table 2. Bottom: learning curves for the fitted GMM, showing the evolution of the train and test Cohen's kappa as a function of the proportion of the training samples used. The shaded areas correspond to the 25–75 percentile range computed over 40 iterations of 70-30% random train-test splitting and bold lines are the medians.

marginal probability. Taking the log of Eq.3 for k_{BS}, we have (the same applies for k_P):

$$-\log[P(k_{BS}|\boldsymbol{x}_i)P(\boldsymbol{x}_i)] = -\log[P(\boldsymbol{x}_i|k_{BS})P(k_{BS})]. \tag{5}$$

Noting that the term $P(\boldsymbol{x}_i|k_{BS})$ on the right hand side is $\mathcal{N}(\boldsymbol{x}_i|\boldsymbol{\mu}_{BS},\boldsymbol{\Sigma}_{BS})$, one can substitute Eq. 2 into the above expression, which yields:

$$-\log[P(k_{BS}|\boldsymbol{x}_i)] - \log[P(\boldsymbol{x}_i)] = \frac{1}{2}(\boldsymbol{x}_i - \mu_{BS})^T \Sigma_{BS}^{-1}(\boldsymbol{x}_i - \mu_{BS}) + \frac{1}{2}\log(|\Sigma_{BS}|) + \frac{D}{2}\log(2\pi) - \log(P(k_{BS})). \tag{6}$$

The quadratic term on the right hand side is the Mahalanobis Distance, which is a distance that uses a Σ^{-1} norm. Hence, it represents the distance between point $\boldsymbol{x}_i$ and the center of the distribution, corrected for correlations and unequal variances in the features space (De Maesschalck et al., 2000). The second term is related to the determinant of the covariance matrix and equals -3.94 for the Blowing Snow component and -2.59 for the Precipitation one. The two last terms are constant and sum to 4.37 (the component proportions were set to 0.5 and $D = 4$). The right side of Eq. 6 is also known as the quadratic discriminant function (QDF, Kimura et al., 1987), commonly noted $g_k(\boldsymbol{x}_i)$. The terms have usually opposite signs, but the minus in front of the logarithm in Eq. 6 is used here to return positive values and facilitate subsequent graphical interpretations. Note that the constant term $\frac{D}{2}\log(2\pi)$ is often removed, but in this case, it ensures that $g_k(\boldsymbol{x})$ is positive, even for a Mahalanobis distance of zero. Figure 8 displays a scatter plot of the quadratic discriminant values of both components for the whole training set. The proposed index is defined as the angle of the vector representing a data point on the scatter plot, normalized by $\frac{\pi}{2}$. It is thus

© Author(s) 2018. CC BY 4.0 License.

computed as follows:

$$\psi = \frac{2}{\pi}\arctan\{\frac{-\log[P(k_P|\boldsymbol{x}_i)P(\boldsymbol{x}_i)]}{-\log[P(k_{BS}|\boldsymbol{x}_i)P(\boldsymbol{x}_i)]}\}. \tag{7}$$

This normalized angle is bounded in $]0,1[$, with values close to 1 and 0 indicating a strong membership to the Blowing Snow and Precipitation clusters, respectively. It is closely related to the asymmetry of the Mahalanobis distances between a point $\boldsymbol{x}_i$ and the centers of the two Gaussian distributions, but corrected by the term $\frac{1}{2}\log(|\Sigma|)$ which is different for the two components. The advantage of using the index in this form, rather than deriving it from the Mahalanobis distances alone, is to respect the decision boundary given by the maximum a posteriori (MAP) rule. This means, a posterior probability of 0.5 yields a ψ index of 0.5. Finally, quantiles 0.9 and 0.1 of the ψ index distributions of the points classified as Precipitation and Blowing Snow, respectively, are retained as thresholds to flag potential mixed images. The idea is to allow, for both classes, 10% of the training set images being flagged as mixed.

To provide the user of the method with an easily readable output, an index of mixing is introduced by linearly rescaling between 0 and 1 the ψ index of the images flagged as mixed. The mixed index also respects the hard clustering assignment boundary at 0.5. A mixed index > 0.5 indicates that the image contains a mix of blowing snow and precipitation particles, but overall being closer to blowing snow and vice versa. Images with a normalized angle outside the two mixed thresholds have a NaN index of mixing and are considered as pure blowing snow particles or pure hydrometeors. Results are provided treating all images independently, but the ψ index is also averaged among the three camera angles to provide a unique value per image identifier as well.

5 Results

The method presented in the previous sections is now tested on the entire Antarctica 17 campaign (January - July 2017) and on the entire Davos campaign (December 2015 - March 2016). About $2 \cdot 10^6$ images for Antarctica and $850'000$ for Davos were classified. Figures 9 and 10 as well as Table 3 present these results. Figure 11 displays the evolution of the normalized angle for a mixed event during the Antarctica 17 campaign.

Table 3. Percentages of MASC images per category

Class	Antartica (Jan - Jul 2017)	Davos (Dec 2015 - Mar 2016)
Pure Blowing snow	36.5%	0.6%
Pure Precipitation	7.2%	39.2%
Mixed Blowing snow	39.1%	20.9%
Mixed Precipitation	17.2%	39.3%

On figure 12, an example of a potential application of the method is illustrated. Histograms and fitted Gamma distributions of *Dmax* for a large subset of images classified as pure blowing snow and pure hydrometeors is shown. Here, the median *Dmax*

© Author(s) 2018. CC BY 4.0 License.

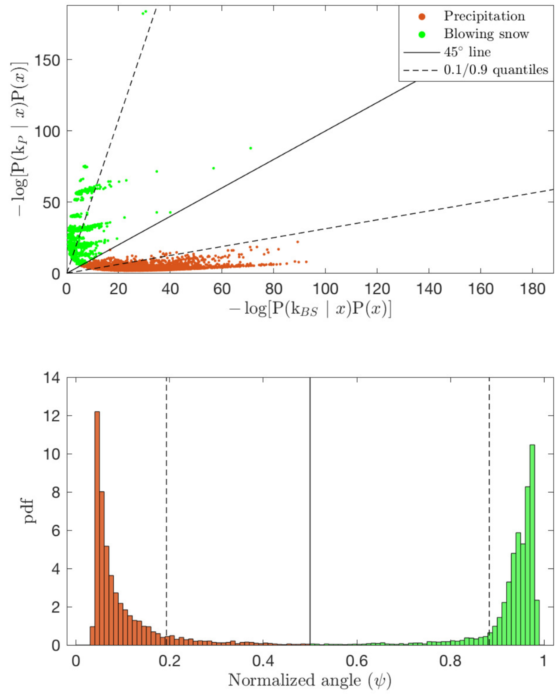

Figure 8. Top: scatter plot of the quadratic discriminant values of both components for the training set. **Bottom**: distributions of the normalized angle for the precipitation and blowing snow subsets and thresholds to identify mixed images

in each image as been used, but all particles from each image could be taken similarly. The units are given in [mm], with the approximation that one pixels ∼33.5 [µm]. Figure 13 shows an example of the output of the algorithm and corresponding images.

6 Conclusions

A novel method to automatically detect images from the MASC instrument corresponding to blowing snow is introduced. The classification is achieved by a two components Gaussian mixture model fitted on a subset of 8450 representative images from field campaigns in Antarctica and Davos, Switzerland. To classify the images, the method computes four selected descriptors via image processing. The descriptors were selected to be relevant for discriminating between blowing snow particles and hydrometeors as well as to be robust to image processing artifacts. The GMM posterior probabilities are mapped into a new index that allows a better identification of mixed images and a flag signals whether an image is classified as pure hydrometeor, pure blowing snow or mixed. For mixed images, an index between 0 and 1 indicates if the image is closer to blowing snow or

© Author(s) 2018. CC BY 4.0 License.

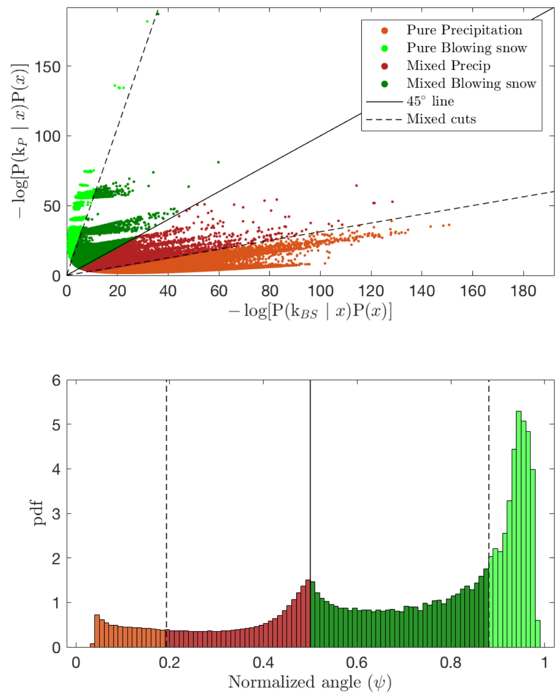

Figure 9. Top: scatter plot of the quadratic discriminant values of both components for the entire Antarctica 17 campaign. **Bottom**: distribution of the normalized angle and corresponding classification.

precipitation. The outputs are provided for each image independently or for each triplet of images (i.e. information combined over the three cameras of the MASC).

Results from a measurement campaign conducted at the Dumont d'Urville station on the coast of East Antarctica from January to July 2017 suggest that about 75% of the images are affected by blowing snow and that about 36% may be composed of blowing snow particles only (Table 3). The results also suggest that 57% of the images could be made of a mix of blowing snow and precipitation particles, which support findings that in Antartica, blowing snow is frequently combined with precipitation (Gossart et al., 2017). Moreover, time series of the classified images highlight that blowing snow strongly relies upon fresh snow availability and often starts shortly after the beginning of precipitation (Fig.11), which is also consistent with conclusions from Gossart et al. (2017). Results from images taken inside a Double Fence Intercomparison Reference in Davos at 2540 m a.s.l between December 2015 and March 2016, indicate that despite the sheltering structure, about 60% of the images could be affected to some extent by blowing snow particles from adjacent ledges. In terms of percentage of images, these numbers tend to be quite large, as the image frequency is usually much higher when strong blowing snow occurs. Percentages expressed in terms of time are much smaller.

© Author(s) 2018. CC BY 4.0 License.

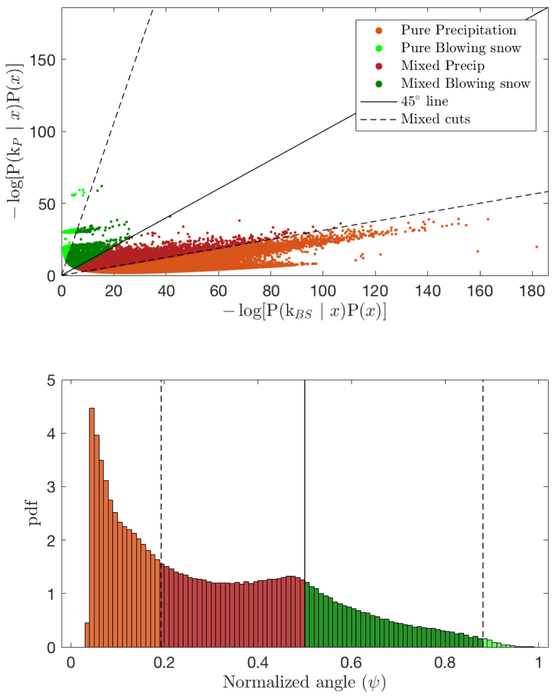

Figure 10. Same as Figure 9 for the entire Davos campaign.

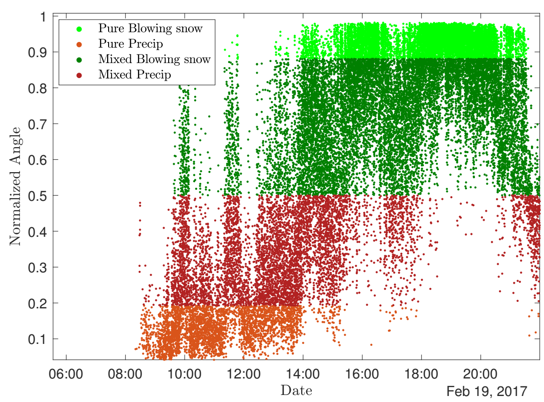

Figure 11. Time series of classified MASC images and according ψ values for a mixed event during the Antarctica 17 campaign.

As the method was developed and tested on fundamentally different campaigns, it may have a general applicability to any other MASC images. However, it should be noted that some descriptors depends on the particular settings (e.g. image size,

© Author(s) 2018. CC BY 4.0 License.

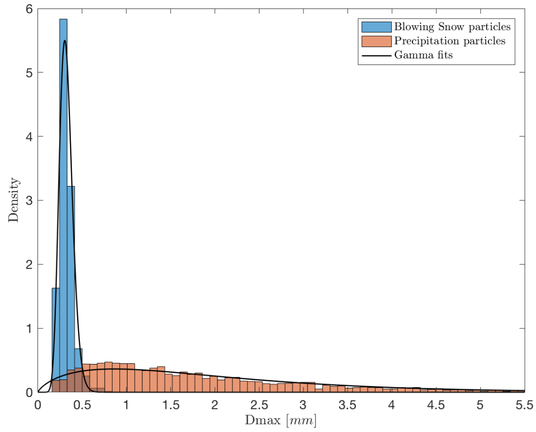

Figure 12. Histograms and fitted Gamma distributions of *Dmax* for images classified as pure blowing snow and pure hydrometeors.

pixel resolution) used during the aforementioned campaigns and a new GMM should be fitted if different settings apply. Further work should be conducted to evaluate if the method can give satisfactory results on images that do not include a timestamp, as the image frequency descriptor could not be utilized. In this case, it could be replaced by one or a couple of other descriptors listed in Table A.1 of Appendix A to strengthen the model. The method could also be adjusted to train a model with a supervised learning algorithm that provides posterior probabilities such as Bayesian classifiers or logistic regression. However, this would imply some effort to improve the training set. An inter-comparison between different machine learning algorithms and the creation of different validation sets could help gain confidence in the results.

The main limitations of the present method are the assumption of normally distributed features through the use of the GMM and the dependency of the method on the defined training set. The latter illustrates the problem of generalization. Some extremely high intensity snowfall events, higher than the ones observed during the Davos and Antarctica campaigns, could be erroneously classified as blowing snow with the current model due to the nature of the descriptors. In this case, higher intensity pure snowfall events should be included in the training set. Another example is the size of the blowing snow particles. During the campaigns in Antarctica, the MASC was set up on a rooftop at 3 m a.g.l. Several studies have demonstrated that the size of blowing snow particles tends to decrease with height (Nishimura et al., 2014; Nishimura and Nemoto, 2005). Consequently, blowing snow particles on images from a MASC that would have been set up at much higher or lower heights may have a bias relative to the fitted Gaussian distribution of the Blowing Snow cluster for *Dmax*. It is thus recommended to follow the procedure described in this article and fit a new model, if the one provided does not perform well in other contexts.

Appendix A: Feature extraction

The Cryosphere Discuss., https://doi.org/10.5194/tc-2018-248
Manuscript under review for journal The Cryosphere
Discussion started: 13 December 2018
© Author(s) 2018. CC BY 4.0 License.

date_vec_unique	1 ID	2 Label	3 Normalized_Angle	4 Flag_mixed
25/03/2016 16:56:35	7383	1	0.7422	0.8178
25/03/2016 16:56:39	7384	0	0.1590	NaN
25/03/2016 16:56:39	7385	1	0.5659	0.5865
25/03/2016 16:56:40	7386	0	0.1437	NaN
25/03/2016 16:56:42	7387	0	0.1920	NaN
25/03/2016 16:56:42	7388	0	0.2260	0.0537

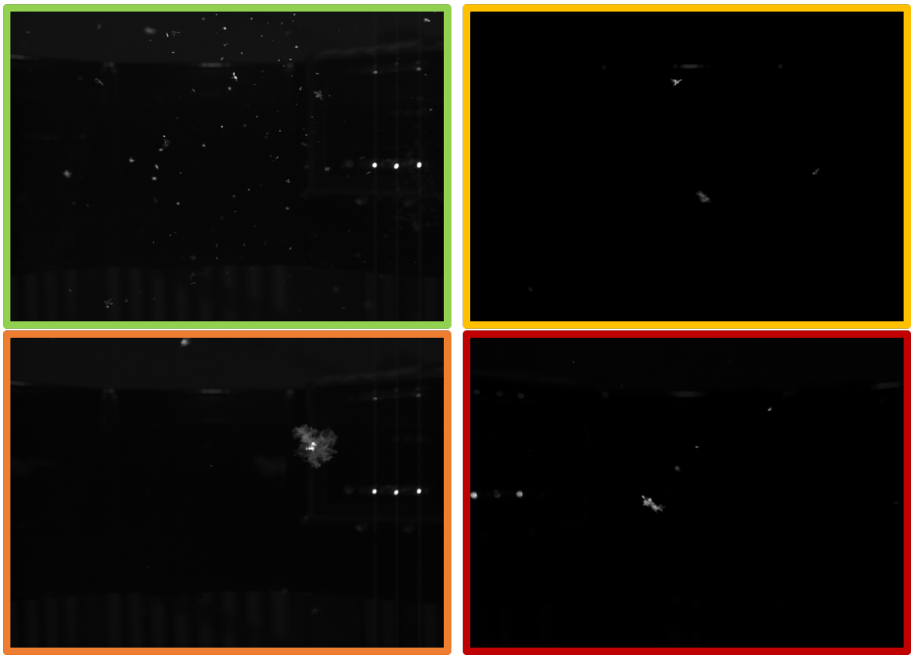

Figure 13. Consecutive MASC images from Davos and their respective classification label, normalized angle and mixing index. Label 1 is for blowing snow. A NaN mixing index means pure hydrometeor (or pure blowing snow). A mixing index close to 1 (top left image) means that it is near pure blowing snow, while a value close to 0 (bottom right image) indicate proximity to pure precipitation.

© Author(s) 2018. CC BY 4.0 License.

Table A1. Full list of all computed descriptors. Descriptors related to each particle are transformed into a single descriptor for the image (right column). Selected ones are shown with an asterisk

Image frequency*	-
Number of particles detected in the image	-
Distance to connect all particles	-
Number of particles smaller than a given threshold	-
Ratio of the area represented by all particles to the area of the smallest polygon encircling them	-
Cumulative distance transform*	-
Maximum diameter*	quantiles 0-1, Moments 1-5
Particle area	quantiles 0-1, Moments 1-5
Particle convexe area	quantiles 0-1, Moments 1-5
Particle perimiter	quantiles 0-1, Moments 1-5
Fractal Index (FRAC), Fractal Index squared*	quantiles 0-1, Moments 1-5
Gravelius compactness coefficient (ratio of the perimeter to the one of a circle with equivalent area)	quantiles 0-1, Moments 1-5

© Author(s) 2018. CC BY 4.0 License.

Appendix B: Image processing issues

The median filter may perform not satisfactorily, for instance when the background luminosity is changing rapidly (see Fig. B1).

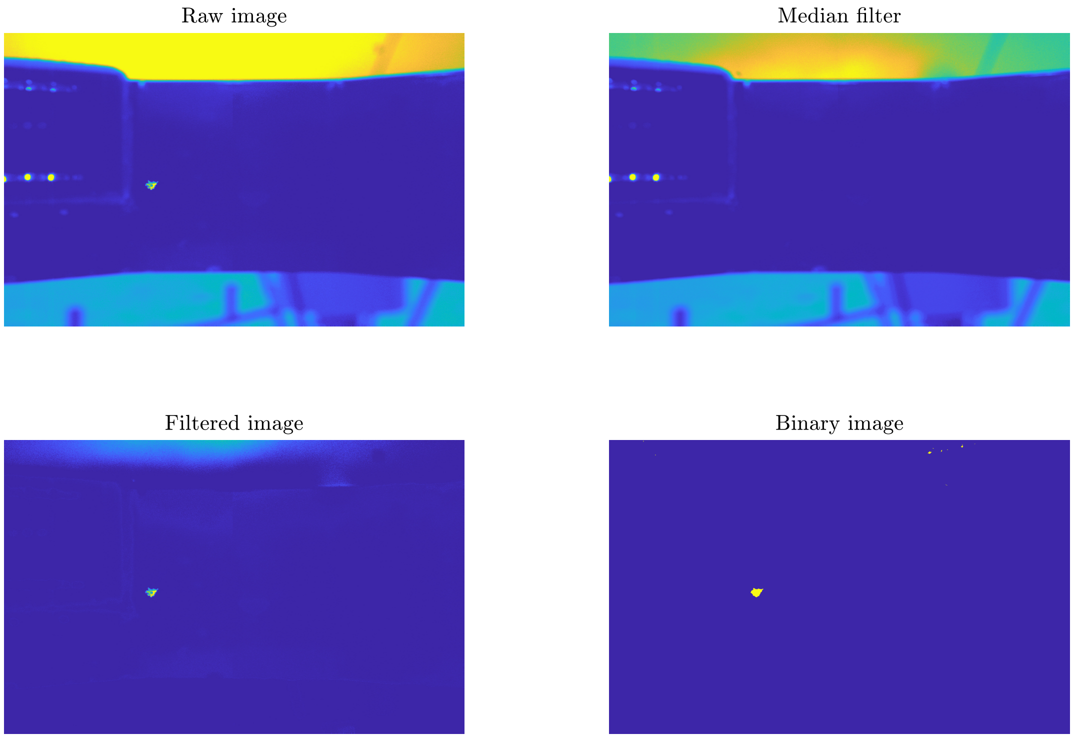

Figure B1. Raw image, median filter, filtered image and final binary image for an example where the median filter does not perform well due to changes in sky luminosity. Some artifacts appear on the top right of the binary image

Similarly, large precipitaiton particles may split or appear as such in the MASC images (see Fig. B2), leading to potential biases in the number of detected particles.

Code availability. TEXT

Data availability. TEXT

Code and data availability. The MASC images and the matlab codes used in the present work are available upon request to the authors.

The Cryosphere Discuss., https://doi.org/10.5194/tc-2018-248
Manuscript under review for journal The Cryosphere
Discussion started: 13 December 2018
© Author(s) 2018. CC BY 4.0 License.

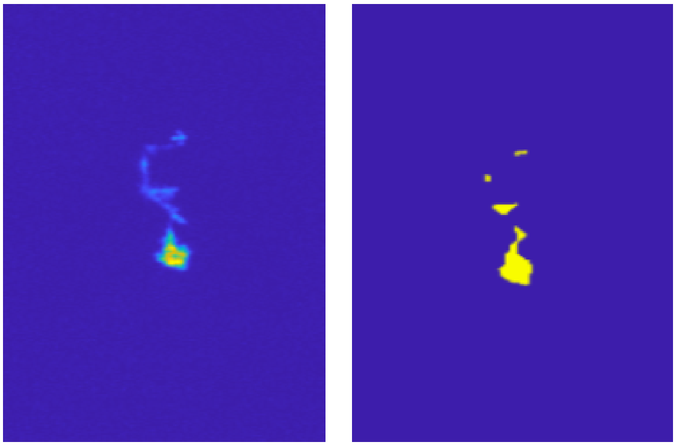

Figure B2. A precipitation particle split into fragments that could be confused with blowing snow particles. The Cumulative distance transform descriptor is much less affected by such image processing issues than the number of particles.

Sample availability. TEXT

Author contributions. TEXT

Competing interests. The authors have no competing interests

Disclaimer. TEXT

Acknowledgements. The authors are thankful to Yves-Alain Roulet and Jacques Grandjean from MeteoSwiss, as well as to Claudio Dùran from IGE Grenoble and to the technical staff at the Dumont d'Urville station for their help to collect the set of MASC images used in this study. CP was supported by the Swiss National Science Foundation (grant 200020_175700).

The Cryosphere Discuss., https://doi.org/10.5194/tc-2018-248
Manuscript under review for journal The Cryosphere
Discussion started: 13 December 2018
© Author(s) 2018. CC BY 4.0 License.

References

Bintanja, R.: Snowdrift sublimation in a katabatic wind region of the Antarctic ice sheet, J. Appl. Meteorol., 40, 1952–1966, https://doi.org/10.1175/1520-0450(2001)040<1952:SSIAKW>2.0.CO;2, 2001.

Box, J. E., Bromwich, D. H., Veenhuis, B. A., Bai, L.-S., Stroeve, J. C., Rogers, J. C., Steffen, K., Haran, T., and Wang, S.-H.: Greenland ice sheet surface mass balance variability (1988–2004) from calibrated polar MM5 output, J. Climate, 19, 2783–2800, 2006.

Byrt, T., Bishop, J., and Carlin, J. B.: Bias, prevalence and kappa, J. Clin. Epidemiol., 46, 423–429, 1993.

Das, I., Bell, R. E., Scambos, T. A., Wolovick, M., Creyts, T. T., Studinger, M., Frearson, N., Nicolas, J. P., Lenaerts, J. T. M., and van den Broeke, M. R.: Influence of persistent wind scour on the surface mass balance of Antarctica, Nat. Geosci., 6, 367–371, https://doi.org/10.1038/NGEO1766, 2013.

De Maesschalck, R., Jouan-Rimbaud, D., and Massart, D. L.: The Mahalanobis distance, Chemometr. Intell. Lab., 50, 1–18, 2000.

Déry, S. J. and Yau, M.: Large-scale mass balance effects of blowing snow and surface sublimation, J. Geophys. Res., 107, ACL–8, 2002.

Ehbrecht, M., Schall, P., Ammer, C., and Seidel, D.: Quantifying stand structural complexity and its relationship with forest management, tree species diversity and microclimate, Agr. and Forest Meteor., 242, 1–9, 2017.

Gallée, H., Guyomarc'h, G., and Brun, E.: Impact of snow drift on the Antarctic ice sheet surface mass balance: possible sensitivity to snow-surface properties, Bound.-Lay. Meterol., 99, 1–19, 2001.

Garrett, T. J., Fallgatter, C., Shkurko, K., and Howlett, D.: Fall speed measurement and high-resolution multi-angle photography of hydrometeors in free fall, Atmos. Meas. Tech., 5, 2625–2633, https://doi.org/10.5194/amt-5-2625-2012, 2012.

Garrett, T. J., Yuter, S. E., Fallgatter, C., Shkurko, K., Rhodes, S. R., and Endries, J. L.: Orientations and aspect ratios of falling snow, Geophys. Res. Lett., 42, 4617–4622, 2015.

Genthon, C., Berne, A., Grazioli, J., Alarcon, C. D., Praz, C., and Boudevillain, B.: Precipitation at Dumont d'Urville, Adélie Land, East Antarctica: the APRES3 field campaigns dataset, Earth Syst. Sci. Data, 10, 1605–1612, https://doi.org/10.5194/essd-10-1605-2018, 2018.

Goodison, B. E., Louie, P. Y., and Yang, D.: WMO solid precipitation measurement intercomparison, World Meteorological Organization Geneva, Switzerland, 1998.

Gordon, M. and Taylor, P. A.: Measurements of blowing snow, Part I: Particle shape, size distribution, velocity, and number flux at Churchill, Manitoba, Canada, Cold Reg. Sci. Technol., 55, 63–74, 2009.

Gossart, A., Souverijns, N., Gorodetskaya, I. V., Lhermitte, S., Lenaerts, J. T., Schween, J. H., Mangold, A., Laffineur, Q., and van Lipzig, N. P.: Blowing snow detection from ground-based ceilometers: application to East Antarctica, The Cryosphere, 11, 2755, 2017.

Grazioli, J., Genthon, C., Boudevillain, B., Duran-Alarcon, C., Del Guasta, M., Madeleine, J.-B., and Berne, A.: Measurements of precipitation in Dumont d'Urville, Adélie Land, East Antarctica, The Cryosphere, 11, 1797–1811, https://doi.org/10.5194/tc-11-1797-2017, https://www.the-cryosphere.net/11/1797/2017/, 2017.

Kennedy, P., Thurai, M., Praz, C., Bringi, V., Berne, A., and Notaroš, B. M.: Variations in Snow Crystal Riming and Z DR: A Case Analysis, J. Appl. Meteor. Clim., 57, 695–707, 2018.

Kimura, F., Takashina, K., Tsuruoka, S., and Miyake, Y.: Modified quadratic discriminant functions and the application to Chinese character recognition, IEEE T. Pattern Anal., pp. 149–153, 1987.

Lehning, M. and Fierz, C.: Assessment of snow transport in avalanche terrain, Cold Reg. Sci. Technol., 51, 240–252, 2008.

Lenaerts, J. T. M. and van den Broeke, M. R.: Modeling drifting snow in Antarctica with a regional climate model: 2. Results, J. Geophys. Res., 117, https://doi.org/10.1029/2010JD015419, 2012.

© Author(s) 2018. CC BY 4.0 License.

Leonard, K. C., Tremblay, L.-B., Thom, J. E., and MacAyeal, D. R.: Drifting snow threshold measurements near McMurdo station, Antarctica: A sensor comparison study, Cold Reg. Sci. Technol., 70, 71–80, 2012.

Lesins, G., Bourdages, L., Duck, T., Drummond, J., Eloranta, E., and Walden, V.: Large surface radiative forcing from topographic blowing snow residuals measured in the High Arctic at Eureka, Atmos. Chem. Phys., 2009.

McGarigal, K. and Marks, B. J.: Spatial pattern analysis program for quantifying landscape structure, Tech. Rep. Gen. Tech. Rep. PNW-GTR-351, US Department of Agriculture, Forest Service, Pacific Northwest Research Station, 1995.

McLachlan, G. J. and Basford, K. E.: Mixture models: Inference and applications to clustering, vol. 84, Marcel Dekker, 1988.

Moerland, P.: Mixture models for unsupervised and supervised learning, 2000.

Mott, R. and Lehning, M.: Meteorological Modeling of Very High-Resolution Wind Fields and Snow Deposition for Mountains, JHM, 11, 934–949, https://doi.org/10.1175/2010JHM1216.1, 2010.

Murphy, K. P.: Machine Learning: A Probabilistic Perspective, MIT Press, 2012.

Nishimura, K. and Nemoto, M.: Blowing snow at Mizuho station, Antarctica, Philos. T. Roy. Soc. A, 363, 1647–1662, 2005.

Nishimura, K., Yokoyama, C., Ito, Y., Nemoto, M., Naaim-Bouvet, F., Bellot, H., and Fujita, K.: Snow particle speeds in drifting snow, J. Geophys. Res., 119, 9901–9913, 2014.

Palm, S. P., Yang, Y., Spinhirne, J. D., and Marshak, A.: Satellite remote sensing of blowing snow properties over Antarctica, J. Geophys. Res., 116, –, https://doi.org/10.1029/2011JD015828, 2011.

Pomeroy, J. and Li, L.: Prairie and arctic areal snow cover mass balance using a blowing snow model, J. Geophys. Res., 105, 26 619–26 634, 2000.

Praz, C., Roulet, Y.-A., and Berne, A.: Solid hydrometeor classification and riming degree estimation from pictures collected with a Multi-Angle Snowflake Camera, Atmos. Meas. Tech., 10, 1335–1357, https://doi.org/10.5194/amt-10-1335-2017, 2017.

Rasmussen, R., Baker, B., Kochendorfer, J., Meyers, T., Landolt, S., Fischer, A. P., Black, J., Thériault, J. M., Kucera, P., Gochis, D., Smith, C., Nitu, R., Hall, M., Ikeda, K., and Gutmann, E.: How well are we measuring snow: The NOAA/FAA/NCAR winter precipitation test bed, Bull. Amer. Meteor. Soc., 93, 811–829, https://doi.org/10.1175/BAMS-D-11-00052.1, 2012.

Scaff, L., Yang, D., Li, Y., and Mekis, E.: Inconsistency in precipitation measurements across the Alaska–Yukon border, The Cryosphere, 9, 2417–2428, 2015.

Scarchilli, C., Frezzotti, M., Grigioni, P., De Silvestri, L., Agnoletto, L., and Dolci, S.: Extraordinary blowing snow transport events in East Antarctica, Clim. Dynam., 34, 1195–1206, https://doi.org/10.1007/s00382-009-0601-0, 2010.

Schweizer, J., Bruce Jamieson, J., and Schneebeli, M.: Snow avalanche formation, Rev. Geophys., 41, 2003.

Shepherd, A., Ivins, E. R., Geruo, A., Barletta, V. R., Bentley, M. J., Bettadpur, S., Briggs, K. H., Bromwich, D. H., Forsberg, R., Galin, N., et al.: A reconciled estimate of ice-sheet mass balance, Science, 338, 1183–1189, 2012.

Winstral, A., Elder, K., and Davis, R. E.: Spatial snow modeling of wind-redistributed snow using terrain-based parameters, J. Hydrometeorol., 3, 524–538, 2002.

Yang, Y., Palm, S. P., Marshak, A., Wu, D. L., Yu, H., and Fu, Q.: First satellite- detected perturbations of outgoing longwave radiation associated with blowing snow events over Antarctica, Geophys. Res. Lett., 41, 730–735, https://doi.org/10.1002/2013GL058932, 2014.